Alternative ice-shelf equilibria determined by ocean environment

JOURNAL OF GEOPHYSICAL RESEARCH: EARTH SURFACE, VOL. 118, 970–981, doi:10.1002/jgrf.20054, 2013

Alternative ice shelf equilibria determined by ocean environment

O. V. Sergienko,[1] D. N. Goldberg,[2] and C. M. Little[3]

Received 18 October 2012; revised 30 January 2013; accepted 7 March 2013; published 10 June 2013.

[1] Dynamic and thermodynamic regimes of ice shelves experiencing weak ($\lesssim$1 m year^{-1}) to strong (~10 m year^{-1}) basal melting in cold (bottom temperature close to the in situ freezing point) and warm oceans (bottom temperature more than half of a degree warmer than the in situ freezing point) are investigated using a 1-D coupled ice/ocean model complemented with a newly derived analytic expression for the steady state temperature distribution in ice shelves. This expression suggests the existence of a basal thermal boundary layer with thickness inversely proportional to the basal melt rate. Model simulations show that ice shelves afloat in warm ocean waters have significantly colder internal ice temperatures than those that float in cold waters. Our results indicate that in steady states, the mass balance of ice shelves experiencing strong and weak melting is controlled by different processes: in ice shelves with strong melting, it is a balance between ice advection and basal melting, and in ice shelves with weak melting, it is a balance between ice advection and deformation. Sensitivity simulations show that ice shelves in cold and warm oceans respond differently to increase of the ocean heat content. Ice shelves in cold waters are more sensitive to warming of the ocean bottom waters, while ice shelves in warm waters are more sensitive to shallowing of the depth of the thermocline.

Citation: Sergienko, O. V., D. N. Goldberg, and C. M. Little (2013), Alternative ice shelf equilibria determined by ocean environment, *J. Geophys. Res. Earth Surf.*, *118*, 970–981, doi:10.1002/jgrf.20054.

1. Introduction

[2] Antarctic ice shelves exist in a variety of oceanographic thermal regimes: from "cold" regime exemplified by the Filchner-Ronne and Ross ice shelves, where the sub–ice shelf water is dominated by high-salinity shelf water (HSSW) at ~−1.8°C [e.g., *Jacobs et al.*, 1979; *Nicholls et al.*, 2001], to "warm" regime exemplified by the Pine Island Glacier (PIG) or George VI ice shelves, where the sub–ice shelf water is dominated by circumpolar deep water (CDW) (~1.2°C) [e.g., *Jacobs et al.*, 2011; *Jenkins and Jacobs*, 2008]. Ice shelves in "cold" oceans generally experience a range of basal conditions, from freezing to weak melting ($\lesssim$1 m year^{-1}), and typically melt near the grounding line [e.g., *Engelhardt and Determann*, 1987; *Jenkins and Doake*, 1991; *Nicholls et al.*, 2001; *Joughin and Padman*, 2003; *Jenkins et al.*, 2006]. In contrast, observations of ice shelves in "warm" ocean environments suggest widespread basal melting with average melt rates up to tens of meters per year [e.g., *Jenkins and Jacobs*, 2008; *Jacobs et al.*, 2011]. Given that ice shelves in both types of oceanic environment are fed by ice streams with similar thermodynamics and dynamics, one is led to the question of to what extent is the state (geometric, dynamic, and thermodynamic) of an ice shelf determined by the oceanic environment in which it floats.

[3] Knowledge of the thermal state of today's ice shelves is primarily restricted to those in "cold" ocean conditions, where in situ borehole temperature measurements have been taken [*Zotikov et al.*, 1980; *Orheim et al.*, 1990]. This thermal state also has impact on ice shelf melting and flow, with flow being dependent on ice temperature through ice viscosity [e.g., *MacAyeal and Thomas*, 1986; *Humbert et al.*, 2005]. However, it remains unclear what thermal regimes ice shelves should have in different ocean environments, and to what degree differences in basal melting rates can be attributed to differences in ocean environment or to differences in ice shelf thermal state.

[4] Basal mass balance remains one of the most difficult to determine unknowns in overall shelf mass balance. Its direct observation is technically and logistically challenging [*Jenkins et al.*, 2006]. The majority of basal mass balance estimates come from either oceanographic measurements [e.g., *Jacobs et al.*, 1979, 2011] or remote-sensing observations [e.g., *Joughin and Padman*, 2003; *Shepherd et al.*, 2003, 2004]. The former provide bulk values (i.e., area averaged), and the latter rely on a set of assumptions (e.g., steady state) and other measurements (e.g., ice thickness and surface accumulation rates) that might have insufficient resolution and are often taken during different time periods. These indirect estimates lack details necessary to establish the effect of surrounding oceans on ice shelves, to attribute causes of observed ice shelf changes, and to make projections of the possible ice shelf changes under different climate conditions.

Additional supporting information may be found in the online version of this article.

[1]GFDL/AOS Princeton University, Princeton, New Jersey, USA.
[2]Department of Earth, Atmospheric and Planetary Sciences, MIT, Boston, Massachusetts, USA.
[3]Woodrow Wilson School of Public and International Affairs, Princeton University, Princeton, New Jersey, USA.

Corresponding author: O. V. Sergienko, GFDL/AOS Princeton University, 201 Forrestal Road, Princeton, NJ 08540, USA. (osergien@princeton.edu)

2169-9003/13/10.1002/jgrf.20054

[5] This study aims to establish fundamental aspects of the ice shelf/sub–ice shelf cavity systems that are determined by differences in the ambient oceanographic conditions. We investigate the coupled geometric, dynamic, and thermodynamic behavior of ice shelves in the two "classical" oceanographic environments: one dominated by "cold" high-salinity shelf water (−1.8°C) and the other dominated by "warm" circumpolar deep water (1.2°C). The main question considered in this study is the following: if two identical ice streams flow into "cold" and "warm" oceans, how different are the ice shelves that they produce? We use a 1-D coupled ice shelf/ocean model and a newly derived analytic expression for the steady state temperature distribution in ice shelves experiencing basal melting to conduct our investigations. The coupled model includes an ice flow model and a plume ocean model. We investigate the following aspects of the ice shelf/sub–ice shelf cavity system: ice shelf morphology, melt rate distribution, ice shelf dynamic and thermodynamic states, and their mutual effects. Also, we consider the implications of this coupled interaction on modeling approaches. Finally, we explore sensitivities of this system to oceanic and grounded ice conditions. We investigate the effects of increase in the ocean heat content in two ways: through warming the bottom ocean water and through shallowing the depth of the thermocline.

2. Advection-Dominated Ice Shelf Temperature

[6] Ice shelves are the fast-flowing components of ice sheets, moving at hundreds to thousands of meters per year. Consequently, their thermal state is dominated by heat advection rather than diffusion. We show this below by comparing characteristic scales of different terms in the advection-diffusion equation governing ice shelf temperature. We restrict our analysis to ice shelves in steady state, with fixed, time-independent geometry. Ablation/accumulation at the top surface, as well as variations in the surface temperature are disregarded to simplify the analysis and restrict it to basal melting; however, the analysis can easily be extended to account for these factors. A justification for these simplifications in the present study will be provided in section 4.

[7] For ice shelves that flow in one horizontal direction only, the steady state heat equation is as follows:

$$uT_x + wT_z = \kappa_i T_{zz} \tag{1}$$

where x and z are the horizontal and vertical coordinates, $T(x,z)$ is ice temperature, u and w are ice horizontal and vertical velocity components, κ_i is the thermal diffusivity of ice (assumed to be independent of density and temperature), and subscripts x and z denote the partial derivatives with respect to x and z, respectively. Viscous heating and horizontal diffusion are disregarded due to their negligible effects [e.g., *MacAyeal and Thomas*, 1986]. Boundary conditions are as follows:

$$T(x,s) = T_s \tag{2a}$$

$$T(x,b) = T^*(x) \tag{2b}$$

$$T(0,z) = T_g(z) \tag{2c}$$

where s and b are the elevations of the top and bottom surfaces of the ice shelf, T_s is temperature at the ice shelf top surface (assumed to be uniform), $T_g(z)$ is the ice shelf temperature profile at the grounding line, $x=0$, and $T^*(x)$ is the seawater freezing temperature that depends on in situ seawater salinity S and pressure p

$$T^*(S,p) = c_1 S^*(x) + c_2 + c_3 p(x), \tag{3}$$

where c_1, c_2, and c_3 are empirical constants.

[8] Other than within a few ice thicknesses of the grounding line and ice front, the horizontal ice shelf velocity components do not depend on the vertical coordinate z [*MacAyeal*, 1989]; therefore, the vertical ice shelf velocity component varies linearly with z as a result of ice incompressibility (firn densification is disregarded for simplicity). These facts, and the use of a stretched vertical coordinate

$$\zeta = \frac{z-b}{H}, \tag{4}$$

where $H = s - b$ is ice thickness, allow equation (1) to be written in the following form [e.g., *MacAyeal and Thomas*, 1986; *Hindmarsh*, 1999; *MacAyeal*, 1997, p. 270–273]:

$$uT_x - \frac{T_\zeta}{H}\left[\zeta\dot{a} + (1-\zeta)\dot{b}\right] = \frac{\kappa_i}{H^2} T_{\zeta\zeta} \tag{5}$$

where $\dot{a}$ is the surface accumulation rate (indicating negative for ablation) and $\dot{b}$ is the basal melt rate (positive for melting). We assume that the surface ablation rate $\dot{a}$ is negligible compared to basal melt rate $\dot{b}$; therefore, the first term in the square brackets on the left-hand side is set to zero.

[9] Characteristic values for u, H, $\dot{b}$, and L are 300 m year^{-1}, 1000 m, 1 m year^{-1}, and 300 km, respectively. With the ice thermal diffusivity $\kappa_i = 36$ m^2 year^{-1}, the right-hand side of equation (5) that represents heat diffusion is at least 2 orders of magnitude smaller than both terms in the left-hand side, and can therefore be neglected. The Peclet number, $Pe = \frac{H^2 u}{L\kappa_i}$, for ice shelves with basal melting is much greater than 1, indicating that heat advection is the dominant process. The ice shelf temperature solution under these circumstances is as follows:

$$T(x,\zeta) = T_g[\xi(x,\zeta)] + \left\{T^*(x) - T_g[\xi(x,0)]\right\} e^{-\frac{bH\zeta}{\kappa_i}\zeta}. \tag{6}$$

where $T_g[\zeta] \equiv T_g(\zeta)$, $T^*(x)$ is determined by equation (3),

$$\xi(x,\zeta) = 1 - \frac{1-\zeta}{q_g} q(x), \tag{7a}$$

$$q(x) = u(x)H(x), \tag{7b}$$

and where $q(x)$ and q_g are the ice fluxes at a point x and at the grounding line, respectively. A derivation of this solution is presented in Appendix A. The characteristic thickness of the thermal boundary layer, represented by the exponential term on the right-hand side of equation (6), is $\sim \frac{\kappa_i}{\dot{b}}$, which is on the order of a few meters for basal melt rates on the order of a few meters per year (10 m for a 3.6 m year^{-1} melt rate), and less than a meter when basal melting is strong (~0.5 m for a 70 m year^{-1} melt rate).

[10] The mass and energy balance at the ice shelf bottom surface (the Stefan condition) that determines the melt rate is as follows [*Holland and Jenkins*, 1999]:

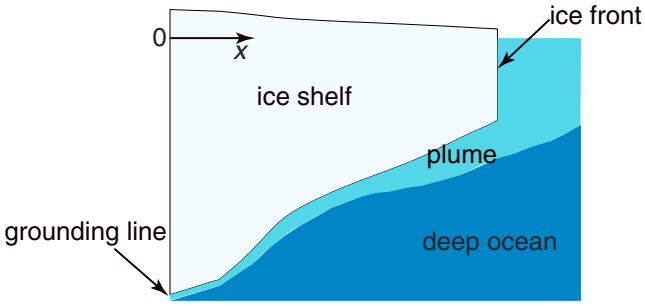

Figure 1. Model geometry.

$$\rho_w \gamma_S (S_o(x) - S^*) = \dot{b} S^* \tag{8a}$$

$$k_i T_z|_{z=b} - \gamma_T \rho_w c_w (T|_{z=b} - T_o) = L_i \rho \dot{b} \tag{8b}$$

where k_i is heat conductivity of ice, $\gamma_{S,T}$ are the salt and heat transfer coefficient at the ice-ocean interface (defined below), ρ_w is seawater density, c_w is the specific heat capacity of seawater, $S_o(x)$ and $T_o(x)$ are the ocean mixed layer salinity and temperature, respectively, and L_i is the ice latent heat of fusion. The first term of equation (8b) is the heat flux into ice above the bottom, and the second term is the heat flux from the ocean mixed layer. The expression for temperature in the ice shelf represented by equation (6) allows computation of the heat flux into ice. Substituting the heat flux expression into equation (8b) and rearranging terms, we arrive at the following expression:

$$\{\gamma_T \rho_w c_w [T_o(x) - T^*] = \rho \dot{b} \{c_i (T^* - T_g[\xi(x,0)]) + L_i\} - \frac{k_i}{H} \frac{q(x)}{q_g} T_{g\zeta}[\xi(x,0)] \tag{9}$$

where c_i is the specific heat capacity of ice. This expression has a simple heat balance interpretation. Heat stored in the ocean mixed layer (the left-hand side) is available to do three things: (1) warm the ice shelf thermal boundary layer to the in situ melting point, T^*; (2) melt that ice that has reached the in situ melting point (terms in the first curly brackets on the right-hand side of equation (9)); and (3) conduct into the colder ice above (the last term on the right-hand side of equation (9)).

3. Model Formulation and Experiments

[11] We consider an ice shelf flowing in one horizontal dimension floating on its cavity where the ocean circulation can be simulated as a two-layer system: an immobile, deep ambient layer with horizontally uniform stratification lies beneath a buoyancy-driven plume layer (Figure 1). To investigate steady state configurations of this idealized ice shelf in different oceanographic environments, we couple a 1-D, vertically integrated, and width-averaged ice flow model [e.g., *Dupont and Alley*, 2005] to a 1-D plume model [*Jenkins*, 1991].

3.1. Ice Flow Model

[12] The vertically integrated and horizontally averaged ice shelf momentum balance is as follows:

$$(4\nu H u_x)_x = \rho g H \left(1 - \frac{\rho}{\rho_w}\right) H_x - \begin{cases} \frac{H}{W}\tau_s & \text{confined shelf} \\ 0 & \text{unconfined shelf} \end{cases} \tag{10}$$

where ν is ice viscosity, W is the half width, and τ_s is the side drag to be applied if the ice shelf is confined. Ice viscosity, ν, is strain rate dependent according to Glen's flow law,

$$\nu = \frac{\bar{B}(T)}{2|u_x|^{1-\frac{1}{n}}} \tag{11}$$

where $n = 3$ is the flow law exponent, $\bar{B}(T)$ is the vertically averaged ice stiffness parameter,

$$\bar{B}(T) = \frac{1}{H} \int_b^s dz B[T(z)], \tag{12}$$

and where $B(T) \equiv [A(T)]^{-\frac{1}{n}}$ obeys an Arrhenius-type temperature relationship ($A(T)$ is the Arrhenius parameter) [e.g., *Hooke*, 1981]. We use a linear friction law to describe side drag $\tau_s = -\beta u$, where $\beta = 8 \times 10^8$ Pa s m^{-1}.

[13] The momentum-balance boundary conditions are the kinematic condition at the grounding line, $x = 0$, and the dynamic condition at the ice front, $x = L$,

$$u|_{x=0} = u_0 \tag{13a}$$

$$4\nu H u_x|_{x=L} = \frac{1}{2}\rho g H^2 \left(1 - \frac{\rho}{\rho_w}\right). \tag{13b}$$

[14] The steady state ice shelf mass balance equation is a first-order differential equation

$$q_x \equiv u_x H + u H_x = -\dot{b} \tag{14}$$

with a boundary condition at the grounding line

$$q|_{x=0} = q_g = u_0 H_0 \tag{15}$$

where we use $u_0 = 700$ m year^{-1} and $H_0 = 1400$ m.

[15] We set the ice shelf length $L = 200$ km and specify that the ice shelf thickness at the ice front cannot be less than 50 m. If this thickness is achieved at distance x_{IF} less than 200 km, the ice front is relocated $x = x_{IF}$. In this way, we incorporate a simple calving law that is dependent on ice thickness.

3.2. Plume Model

[16] The plume model, adapted from *Jenkins* [1991], represents the ocean as a two-layer system with an immobile, deep ambient layer with horizontally uniform stratification, and a buoyancy-driven plume boundary layer which evolves according to the mass, momentum, energy, and salt balance equations. These equations are as follows:

$$(UD)_x = \dot{e} + \dot{b} \tag{16a}$$

$$(U^2 D)_x = D\delta\rho_w g H_x - K U^2 \tag{16b}$$

$$(T_o U D)_x = T_a \dot{e} + T^* \dot{b} + \gamma_T (T^* - T_o) \tag{16c}$$

$$(S_o U D)_x = S_a \dot{e} + S^* \dot{b} + \gamma_S (S^* - S_o) \tag{16d}$$

where U, D, T_o, and S_o are velocity, depth, temperature, and salinity of the plume, respectively; $\dot{e}$ is the entrainment rate; $\delta\rho_w$ is the density contrast between the plume and the underlying ambient layer (assumed to be a linear function of temperature and salinity, as in *Jenkins* [1991]); K is the drag coefficient; T_a and S_a are temperature and salinity of the deep ambient layer; and γ_T and γ_S are heat and salt transfer coefficients

$$\gamma_t = \frac{U_*}{2.12\log(U_* D/\nu) + 12.5Pr^{2/3} - 8.68} \tag{17a}$$

$$\gamma_s = \frac{U_*}{2.12\log(U_* D/\nu) + 12.5Sc^{2/3} - 8.68} \tag{17b}$$

where $U_* = K^{1/2}U$ is the friction velocity, and Pr and Sc are Prandtl and Schmidt numbers of seawater, respectively. It should be pointed out that there are two typos in equations (3) and (4) in *Jenkins* [1991]. The second terms on the right-hand side of these equations should be seawater freezing temperature, T^*, and in situ salinity, S^*, respectively, and not plume temperature and salinity, T_o and S_o. Expressions for all other parameters, as well as values of physical constants used in the plume model, are identical to those described by *Jenkins* [1991]. The ocean stratification and ice shelf temperature profiles are described in Appendix B. We limit our study to ice shelves experiencing melting only in order to avoid complications associated with the plume detachment from ice shelves experiencing refreezing.

[17] Novel features in our coupled model are the following: the ability of the ice flow model to explicitly account for ice temperature feedback effects on ice flow through the depth-averaged ice stiffness coefficient $\bar{B}$ in Glen's flow law (equation (12)), and a modified formulation of the Stefan condition in the three-equation formulation of heat and mass conservation at the ice shelf base [*Holland and Jenkins*, 1999]. The ice flow and plume model are coupled geometrically, dynamically, and thermodynamically. Equations (10)–(16), with corresponding boundary conditions, are solved iteratively with the maximum relative tolerance 10^{-4}. All steady states are independent of the initial configurations and are unique. This was verified by running the model with a suite of initial configurations. The obtained steady states were identical within the chosen tolerance.

3.3. Numerical Experiments

[18] We consider two oceanographic environments with a salinity-dependent stratification and bottom water temperatures that represent end members of the thermal regimes typical of Antarctic continental shelves HSSW, in Figure 2a, and CDW, in Figure 3a. The only difference between the HSSW and CDW cases is the temperature of the water at the bottom of the sub–ice shelf cavity, i.e., in the lower ambient layer. The CDW case resembles observations from the front of the PIG [*Jacobs et al.*, 2011, Figure 2]. In both cases, we explore the effects of unconfined and confined ice shelf configurations. As equation (10) shows, wide confined ice shelves with walls far from their centerlines ($W \to \infty$) can be treated as unconfined.

4. Results and Discussion

4.1. Ice Shelf Thermal Structure

[19] The configurations of unconfined ice shelves and their temperature profiles are shown in Figures 2b and 3b, and the bottom surfaces of the confined and unconfined shelves (solid lines) with corresponding melt rates (dashed lines) are shown in Figures 2c and 3c. The magnitudes of melt rates are significantly larger in the CDW case than the observed accumulation rates on Antarctic ice shelves that are typically 10–20 cm year^{-1}. In the HSSW case, melt rates closer to the ice front are of comparable magnitudes or smaller. In order to confirm that our assumption of the zero net surface mass balance does not significantly affect our results, additional simulations for the HSSW case have been performed using a uniform accumulation rate of 30 cm year^{-1}. Figure S1 of the auxiliary material shows that the differences in ice thickness and melt rates are within 6% for the most part of the ice shelf. Thus, our simplification of neglecting surface ablation/accumulation is justified for this study.

[20] In the CDW case, the ice shelf base is steeper than in the HSSW case, and ice thickness at the ice front is less than half the thickness in the HSSW case. The mean ice temperature in the HSSW case is significantly warmer (by more than 3.5 K) than in the CDW case, with a vertical profile close to linear, showing gradual warming from the cold shelf top to the warm base. The thermal boundary layer in the HSSW case is almost an order of magnitude larger than in the CDW case, where most of the ice shelf interior is cold apart from about 10–20 m near the ice shelf bottom where it is warm.

[21] The difference in the behavior of the ice shelves is counterintuitive: the ice shelf floating in warmer CDW is actually colder than floating in the colder HSSW ocean. This counterintuitive result can be understood from the following considerations. Warm ice characteristic of the base of the grounded ice sheet upstream of the grounding line is eroded by strong basal melting concentrated near the grounding line, and colder ice originating from shallower parts of the grounded ice sheet is advected farther downstream, filling the majority of the ice shelf. To demonstrate that removal of the bottom, warm portion of the ice shelf by basal melting has a stronger effect than the heat diffusion from the ocean, we consider a column of ice originated at the grounding line, i.e., we adopt a Lagrangian point of view similar to *MacAyeal and Thomas* [1986] and *MacAyeal and Barcilon* [1988], and follow this ice column as it travels through the ice shelf to the ice front. This column reaches a location x at a time $\tau(x) = \int_0^x \frac{dx'}{u(x')}$ since crossing the grounding line, and the column transit or residence time in the shelf is $\tau(L) = \int_0^L \frac{dx'}{u(x')}$. During this residence time, the maximum thickness of the column that can be affected by thermal diffusion is $H_{\mathrm{th}}(x) \approx 2\sqrt{\kappa_i \tau(x)}$. This thickness of the ice column can be compared with the amount of ice removed from the column by melting, $M_{\mathrm{tot}}(x) = \int_0^x dx' \frac{\dot{b}(x')}{u(x')}$. As Figures 2d and 3d show, the thermal diffusion layer, H_{th}, is less (in the CDW case most significantly) than the thickness of the ice column removed by melting, M_{tot}. Only for unconfined ice shelves in the HSSW case, we find that the thickness of the thermal diffusion layer and amount of ice

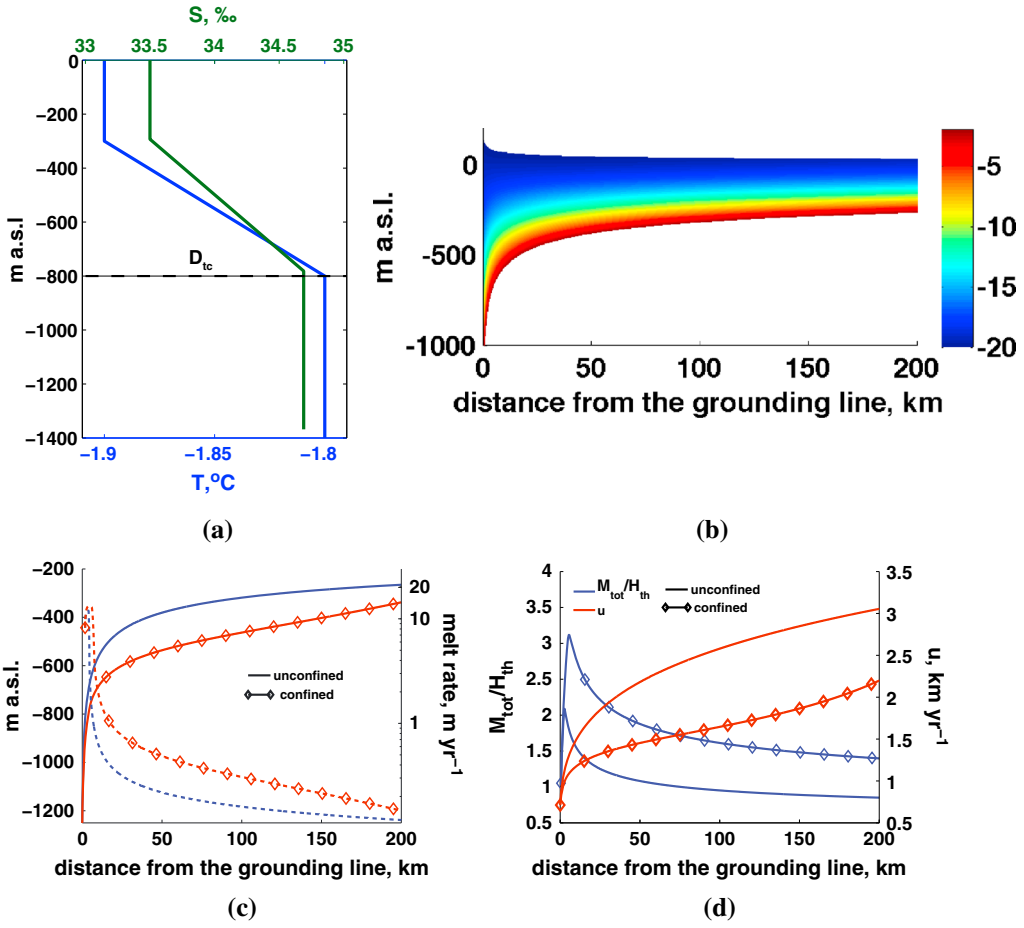

Figure 2. HSSW case. (a) Sea water temperature and salinity. Dashed lined D_{tc} denotes the thermocline depth. (b) Temperature (°C) in the ice shelf. (c) Ice shelf cavity shape (solid lines, left vertical axis) and melt rates (dashed lines, right vertical axis). (d) Ratio of amount of ice melted from an ice column originating at the grounding line, M_{tot}, to thickness of the thermal diffusive layer, H_{th}; the horizontal ice velocity u (km year^{-1}). Lines with no labels are for unconfined shelves, with diamonds for confined shelves. Notice logarithmic scales for melt rates on Figure 2c.

melted from the ice column are comparable and this equality is only applicable to the last 50 km near the ice front. The fact that the thermal diffusion layer is thinner than the amount of ice removed by melting indicates that the internal thermal structure of the ice shelf outside the thermal boundary layer is unaffected by thermal diffusion. In other words, ice shelves with bottom melting can be thought of as fast-moving conveyor belts from which the bottom portion is removed by melting, but where the thermal state of the rest of the ice shelf is unchanged from what it was when the ice was upstream of the grounding line (assuming zero surface accumulation and spatially uniform surface temperature).

4.2. The Direct and Indirect Thermal Effects

[22] The thermal state and temperature distribution of ice shelves have both direct and indirect effects on the ice shelf states. The direct effect is through melt rates, and the indirect effect is through the temperature dependence of ice viscosity. The magnitude of the direct effect on melt rates can be estimated by examining terms of the energy balance at the ice shelf bottom surface (equation (9)). The two terms in curly brackets on the right-hand side of this expression are the amount of heat required to warm the ice shelf thermal boundary layer from its temperature, $T_g[\xi(x,0)]$, to the in situ melting point, T^*, and then required to supply the ice latent heat of fusion, L_i. The specific heat capacity of ice, c_i, is 2.009 kJ kg^{-1} K^{-1}, which value is more than 2 orders of magnitude less than the ice latent heat of fusion, $L_i = 334$ kJ kg^{-1}. The maximum possible temperature difference in the ice shelf is between its top and bottom surfaces, which rarely exceeds 20 K. Hence, the maximum possible error that can be caused by using an incorrect ice shelf temperature value in the first term on the right-hand side of equation (9) is under 10%.

[23] The second term on the right-hand side of equation (9) represents the heat conducted into the ice from the ocean. Inspection of this term shows that $\frac{q(x)}{q_g}$ is always less than 1 due to the fact that, in steady state ice shelves experiencing melting, the highest ice flux is at the grounding line (equation (14)). The strongest temperature gradients observed on ice streams are close to the bottom of the ice column and are ~5×10^{-2} K m^{-1} [*Engelhardt*, 2004]. The first and second terms on the right-hand side of equation (9) are comparable if melt rates are on the order of centimeters per year. For the ice shelves experiencing stronger melting, the first term

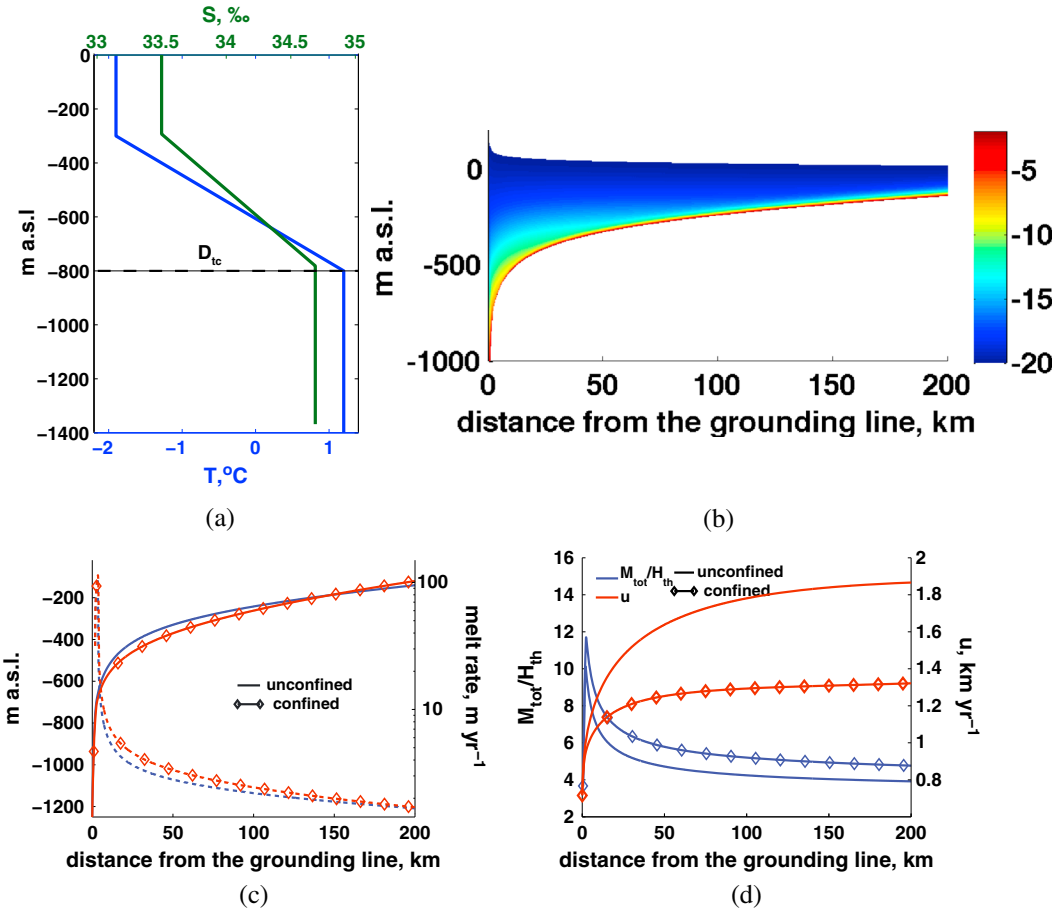

Figure 3. Same as Figure 2 for CDW case. Note change in axis scales in (a), (c), and (d).

dominates, indicating that heat flux into ice can be neglected. These considerations show that the direct effects of the ice shelf temperature distribution do not play a significant role in ice shelves with strong and mild (~0.5–1 m year^{-1}) melting.

[24] The indirect thermal effect on the ice shelf state, through the temperature dependence of ice viscosity, is estimated by comparing the results shown in Figures 2c and 3c with simulations using a spatially uniform ice stiffness parameter $\bar{B}$ equal to a spatially averaged value of $\bar{B}$ obtained in the original simulations (Figures 2c and 3c). Figure 4 shows the relative deviations of the ice stiffness parameter $\bar{B}$ (solid lines, left axis) and relative changes in melt rates (dashed lines, right axis) caused by the indirect thermal effects. The effect of the temperature dependence of ice viscosity is much stronger (~20%) in the CDW case than in the HSSW case, because in the CDW case the ice shelf becomes progressively colder. In addition, $\bar{B}$ experiences larger spatial variations (~15% in the confined ice shelf and ~10% in the unconfined ice shelf) in contrast to the HSSW case, where $\bar{B}$ is more spatially uniform. In the CDW case, simulations with constant $\bar{B}$ yield length-averaged basal melt rates that are overestimated by 18% and 10% in the confined and unconfined configurations, respectively. In the HSSW case, the effects of spatial variations of $\bar{B}$ are significantly smaller: about 3–5% for both the confined and unconfined configurations.

[25] Colder ice is less deformable and more susceptible to fracturing due to the fact that fractures in cold ice are less likely to be arrested than in warm ice [e.g., *Liu and Miller*, 1979]. Hence, ice shelves with strong basal melting that result in a thin boundary layer and a colder ice shelf interior closer to its base might be more susceptible than ice shelves with weak melting to formation and development of basal crevasses. Therefore, it is possible that these ice shelves could be structurally preconditioned to disintegration.

4.3. The Effects of Melting on Ice Shelf Mass Balance and Buttressing

[26] In order to establish the effect of different processes on ice shelf mass balance, we compute two terms on the left-hand side of equation (14) that represent ice deformation (u_xH) and advection (uH_x), respectively. Figures 5a and 5b show the absolute values of these two terms. In the CDW case, the effect of ice deformation rapidly reduces with the distance from the grounding line, and the leading order balance is

$$uH_x \approx -\dot{b}. \tag{18}$$

[27] In the HSSW case, both ice deformation and advection terms are of the same order and are significantly larger than melt rates. Hence, the difference between confined and

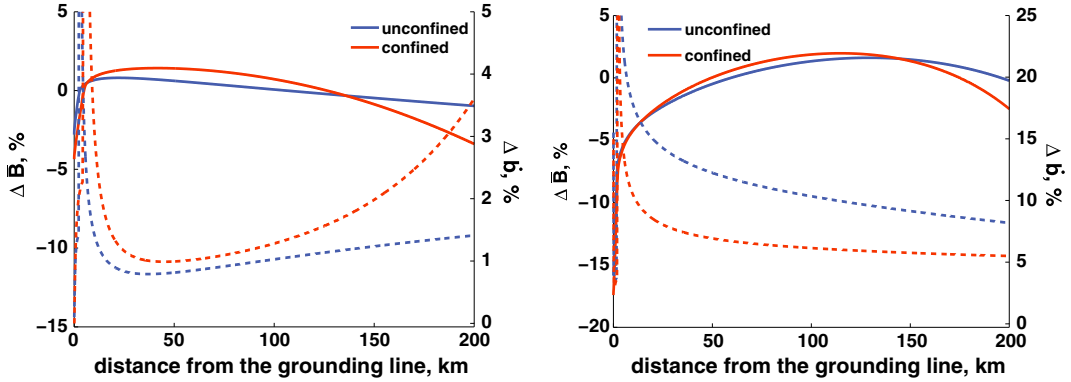

Figure 4. Variations of ice stiffness parameter, $\bar{B}$, from mean value (left axis, solid lines), and deviation of melt rates, $\dot{b}$, (%) (right axis, dashed lines) obtained in simulations using mean value for ice stiffness parameter $\bar{B}$ from the control simulations.

unconfined ice shelf configurations is more pronounced. The leading order balance for this case is as follows:

$$uH_x \approx -u_x H \tag{19}$$

[28] These results indicate the presence of two different mass balance regimes: one is dominated by ice shelf dynamic processes, which is characteristic to ice shelves flowing in cold, HSSW oceanic environments, and the other one is dominated by the ocean circulation processes, which is characteristic to ice shelves in warm, CDW oceanic environments. It should be pointed out that these balances do not hold at or near the grounding line, whose dynamics is not resolved in this study.

[29] Analysis of the confined and unconfined ice shelf configurations in different ocean environments shows that, in the HSSW case (Figure 2c), a confined ice shelf (i.e., with side drag) has a smaller slope near the grounding zone but has a steeper base throughout its length than an unconfined ice shelf. Melt rates at the base of the confined ice shelf are twice as large as those of the unconfined ice shelf. In the CDW case (Figure 3c), the difference between confined and unconfined ice shelves progressively reduces with the distance from the grounding line. The two ice shelf configurations and melt rates become very similar, with melt rates of the confined ice shelf being on average only 10% higher than those of the unconfined ice shelf. This difference between confined and unconfined shelves in the HSSW and CDW raises the question of what the effect of melting might be on buttressing. To evaluate this effect, we analyze the back pressure using the parameter θ_b which is the ratio between the vertically integrated longitudinal and driving stresses.

$$\theta_b = 1 - \frac{4\nu H u_x}{\frac{1}{2}\rho g H^2 \left(1 - \frac{\rho}{\rho_w}\right)} \tag{20}$$

[30] Figure 6 shows the distribution of θ_b for the two ice shelves. In the CDW case, the first half of the ice shelf, within ~100 km downstream of the grounding line, has a smaller θ_b than does the HSSW case. In the second half of the ice shelf, θ_b is larger in the CDW case than in the HSSW case, but the difference is substantially smaller than in the part of the ice shelf that is close to the grounding line. These results indicate that stronger melting does lead to a reduction in the buttressing effect of the ice shelf within the first

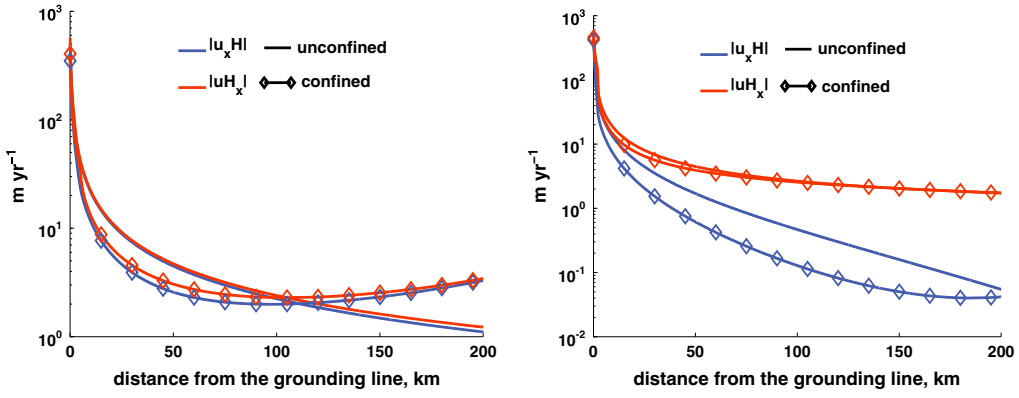

Figure 5. Absolute values of the mass balance terms (the LHS of equation (14)). Lines with no labels are for unconfined ice shelves, with diamonds for confined ice shelves. Notice logarithmic scales on vertical axes.

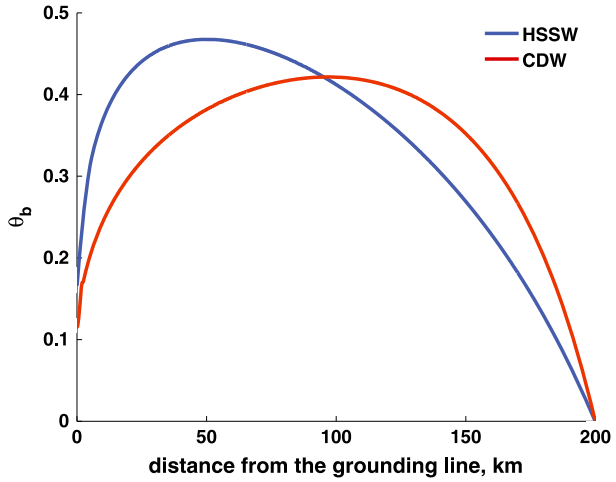

Figure 6. Buttressing factor θ_b defined by equation (20).

100 km from the grounding line, as was proposed earlier [cf. *Schoof*, 2007, for discussion], though, farther from the grounding line, an increase in buttressing is observed, suggesting more complicated response. It should be pointed out that at the grounding line, the difference in θ_b is only 6% larger in the cold, HSSW ocean than in the warm, CDW ocean. In simulations with doubled ice flux at the grounding line (described below), this difference is larger, reaching 23%. Similarities in the back pressure at the grounding line for ice shelves encountering CDW and HSSW indicate that basal melting has less influence on the reduction of buttressing at the grounding line than farther along the ice shelf, provided that the ice flux is constant. We point out, however, that these results are subject to the fixed boundaries and require further investigation with ice flow and ocean circulation models that better represent flows in the vicinity of the grounding lines [e.g., *Gagliardini et al.*, 2010; *Goldberg et al.*, 2012a].

4.4. Coupling Feedbacks

[31] The mutual effects of ice shelf flow and sub–ice shelf circulations neither are a priori known nor can be easily inferred from observations. We assess the strength of these effects by comparing results of the coupled simulations described above to the results of simulations in which ice flow and plume models were uncoupled from each other. In addition, we assess the validity of the two following approaches for computing melt rates that are widely used in ice shelf studies. The first approach involves estimates of melt rates from oceanographic observations of water-mass properties that are indirect indicators of bulk (ice shelf area-averaged) values. They are traditionally used in glaciological studies as representative values of melt rates. However, it is unclear how area-averaged melt rates determined by this approach are informative about states of the ice shelf/sub–ice shelf cavity system. The second approach involves use of sub–ice shelf cavity circulation models that are not coupled to ice shelf flows. The main underlying assumption of this approach is that the ice shelf is static. Our experiments aim to establish the limits of applicability of this assumption. We consider only the confined shelf in the HSSW and CDW cases.

[32] In the first experiment, we compute ice shelf configurations with the uncoupled ice flow model using average melt rates computed in the coupled simulations. In the CDW case, the difference between coupled and uncoupled simulations with the prescribed uniform melt rates is an order of magnitude larger than in the HSSW case (green solid lines in Figures 7a and 7b). This large difference can be understood by analyzing the dominant balance of the ice shelves in the two different environments (equations (18) and (19)). In the CDW case, to the leading order, the ice shelf thickness gradient (hence, its basal slope) is proportional to melt rate (expression (18)); thus, the spatial distribution of the melt rate plays a dominant role in shaping the ice shelf. Hence, information about spatial variations in melt rates is crucial in

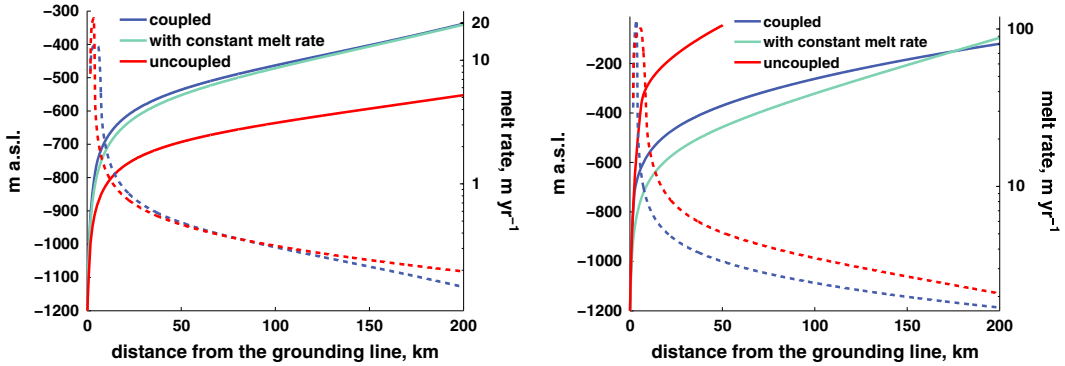

Figure 7. Comparison of coupled and uncoupled computations. Ice shelf cavity shape (solid lines, left vertical axis) and melt rates (dashed lines, right vertical axis). Notice logarithmic scale for melt rates. It is assumed that the ice shelf minimal thickness is 50 m; in some experiments, it was achieved at distances less than the original ice shelf length of 200 km. Dashed red lines are melt rates computed with the uncoupled plume model for corresponding oceanic forcing using the shelf configuration from the opposite panel (e.g., (a) shows melt rates in HSSW environment for an ice shelf configuration shown with blue line in (b)). Solid red lines are ice shelf configurations computed with the uncoupled ice flow model using melt rates shown with red dashed lines. See text for the detailed description of experiments.

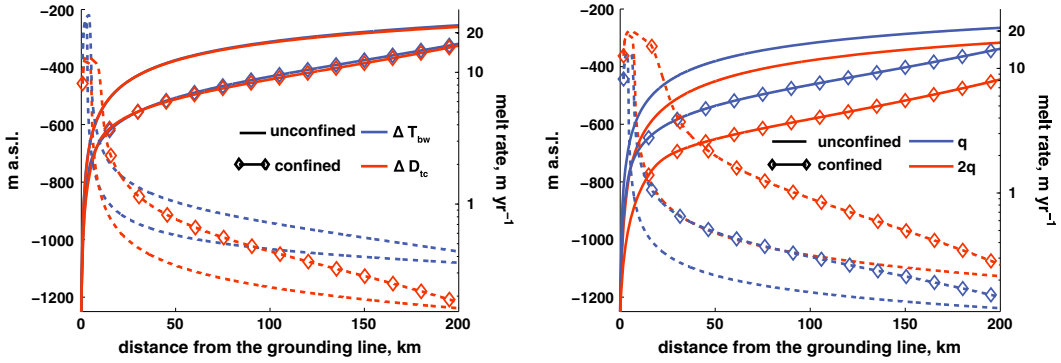

(a) ocean heat content (b) ice flux

Figure 8. HSSW case. (a) Sensitivity to change in the ocean heat content through changes in seawater temperature (ΔT_{bw}, experiment A) and stratification (ΔD_{tc}, experiment B). (b) Sensitivity to doubling of ice flux at the grounding line (experiment C). Ice shelf cavity shape (solid lines, left vertical axis) and melt rates (dashed lines, right vertical axis). Lines with no labels are for unconfined ice shelves, with diamonds for confined ice shelves. Notice logarithmic scale for melt rates.

determining the ice shelf configuration. In contrast to the CDW case, the HSSW case features a leading order mass balance that is between ice shelf deformation and advection (expression (19)), and the spatial distribution of melt rate affects this balance to a lesser degree. These results suggest that the coupling feedbacks are significantly stronger in the warm, CDW oceanic environment.

[33] In the second experiment, we compute melt rates with the uncoupled plume model using the ice shelf configurations from the coupled simulations, but swap the oceanic forcing, i.e., we attempt to simulate what the sub–ice shelf cavity circulation and melt rates would be for an ice shelf from the cold, HSSW ocean environment were it instantaneously subjected to the warm, CDW ocean conditions. Conversely, we simulate what circulation and melt rates would be for an ice shelf flowing in the warm, CDW ocean if suddenly the ocean circulation would bring HSSW into the cavity. In the next step, we use the uncoupled ice flow model and uncoupled melt rates from the previous simulations to compute ice shelf configurations. The melt rates obtained with the plume-only model (red dashed lines in Figure 7) are significantly different from those computed in the coupled simulations. In the HSSW case, the coupled melt rates are significantly higher than the uncoupled ones (about two to three times the length-averaged values), apart from the 2 km area near the grounding line, and near the ice front. Uncoupled simulations of the ice shelf model using the melt rates computed with the uncoupled plume model produce a much thicker ice shelf configuration compared to coupled simulations (red solid line in Figure 7a). In the CDW case, the result is the opposite: the uncoupled melt rates are overall larger by a factor of 3, and near the grounding line are an order of magnitude larger than the coupled ones. Further application of these melt rates in the uncoupled ice shelf model leads to a much shorter and thinner ice shelf (red solid line in Figure 7b).

[34] Such large differences between coupled and uncoupled results, in both HSSW and CDW cases, are due to the strong dependence of the melt rates on the shape of the ice shelf. In the plume flow, the buoyancy force that controls its speed is determined by the shelf slope, the first term on the right-hand side of expression (16b). Thus, there is a strong positive feedback in the ice shelf/sub–ice shelf cavity system: the larger the melt rates, the larger the slope (expression (18)); therefore, the faster the plume flows (expression (16b)), the larger the melt rates become due to their dependence on the plume flow (expression (17a)). In addition, as was mentioned above, all steady states obtained with the coupled model are unique and insensitive to initial conditions. This suggests that, most likely, there is a unique correspondence between a steady state ice shelf configuration, its melt rates, and the ambient oceanic conditions.

[35] These results suggest the following possible limits to the traditional approaches. The use of area-averaged melt rates as representative values for the whole ice shelf is justifiable in circumstances where the dominant mass balance of the ice shelf is between its advection and deformation. Applicability of stand-alone ocean models should be limited to ice shelves that are in dynamic equilibrium with their oceanic environment (i.e., have an approximate zero net mass balance). However, exploration of possible behaviors of such ice shelves in different oceanic environments has to be reserved to coupled investigations.

4.5. Sensitivities to Changes in the Ocean and Grounded Ice Conditions

[36] In this section, we investigate the effects of increasing the ocean heat content (experiments A and B) and ice flux at the grounding line (experiment C) on the ice shelf/sub–ice shelf cavity system. We consider two possibilities for how heat content can increase. The first is the warming of the bottom ocean temperature by 0.5°C (experiment A). The second is the shallowing of the thermocline depth D_{tc} (Figures 2a and 3a) by 100 m, from −800 to −700 m (experiment B). Experiment A mimics the scenario where the source of sub–ice shelf deep water warms. Experiment B mimics the scenario where transport of deep water underneath the ice shelf is increased. Simulations with increased seawater temperature (experiment A) and the thermocline depth (experiment B) show that, in the HSSW case, ice shelf configurations and melt rates are more sensitive to seawater bottom temperature than to the thermocline depth (Figure 8a). Further warming of the already warm bottom water in the CDW case does not affect the shelf configuration and melt rates significantly (Figure 9a,

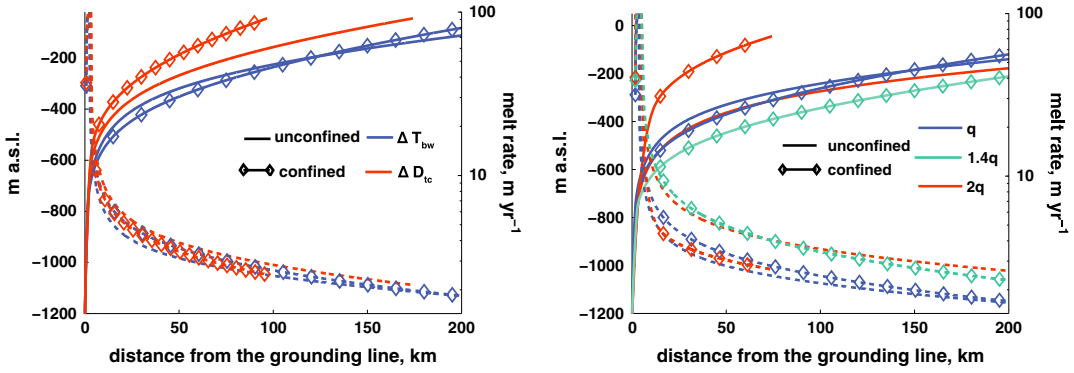

(a) ocean heat content (b) ice flux

Figure 9. Same as Figure 8 for CDW case. In addition to the experiment with double flux for the confined case, an experiment with ice flux 40% larger than the original one has been done (b, green line). It is assumed that the ice shelf minimal thickness is 50 m; in some experiments, it was achieved at distances less than the original ice shelf length of 200 km.

blue lines). However, the shallower thermocline depth leads to very different configuration of both confined and unconfined shelves, which are steeper and shorter than those in the original simulations (Figure 9a, red lines). With the shallower thermocline, the greater part of the ice shelf is exposed to the warm bottom water, and increased melting forces the ice shelf toward a new state where the ice shelf is thinner and steeper.

[37] The high sensitivity to thermocline depth can be understood from examining a leading order mass balance of ice shelves floating in warm waters (expression (18)). In these ice shelves, the basal slope is determined by melt rate; therefore, ice thickness at a location x is $H(x) \approx H_0 - \int_0^x dx' \frac{\dot{b}(x')}{u(x')}$. Since u_x decreases rapidly with the distance from the grounding line (Figure 5b), ice thickness at location x primarily depends on melt rates and their distribution upstream of this location, starting from the grounding line. The ice shelf thins rapidly, and despite the fact that melt rates reduce at shallow depths, the ice shelf gets shorter than in experiment A due to the fact that ice thickness should always be larger than zero or, as in our model setup, larger than 50 m. These results show that ice shelves in cold, HSSW and warm, CDW ocean environments respond differently to an increase ocean heat content, as their individual response depends on the way it is increased. This finding reinforces the evidence that dynamic and thermodynamic feedbacks in ice shelves may alter the relationship between warming of ocean waters and rate of increased melting [e.g., *MacAyeal*, 1984; *Holland et al.*, 2008; *Goldberg et al.*, 2012b].

[38] Results from the simulations with increased ice flux at the grounding line (experiment C; Figures 8b and 9b) show that, in both environments, melt rates of unconfined ice shelves are greater (dashed red lines). This is also the case for a confined ice shelf in the cold ocean environment (Figure 8b). In the warm, CDW ocean environment for the confined ice shelf, doubling ice flux produces a configuration that is much steeper, thinner, and shorter, and has lower melt rates compared to those obtained with the original ice flux. It appears that for ice fluxes ~150% and greater than the original flux, the steady state configurations are very different from those with smaller fluxes. The results of increasing ice flux by 40% for the confined ice shelf (green curves in Figure 9b) are similar to those of the unconfined computations: the ice shelf is thicker and melt rates are larger. The reason for significantly different configurations in circumstances of large ice fluxes at the grounding line seems to be that confined ice shelves cannot transport the increased ice flux as effectively as the unconfined ones, and this results in greater ice thickness and a deeper shelf base. The consequence means that interaction of the ice shelf with warmer ambient waters eroding the ice shelf leads to ice thickness that reduces rapidly along flow to a level where ambient waters are cooler, in situ freezing point is higher, and melt rates are lower.

[39] The response of the confined ice shelves in warm, CDW seawaters to the doubled ice flux is qualitatively similar to the response to increased seawater heat content through change of the thermocline depth (Figures 9a and 9b). Effectively, these experiments are equivalent in the sense of how large a part of the ice shelf is in contact with the warmest water. In experiment B, the shallow thermocline depth brings warmer water into contact with the larger part of the ice shelf. In experiment C, doubled ice flux that caused initial thickening of the ice draft resulted in a larger portion of the ice shelf sitting deeper and interacting with warm waters. However, in contrast to the HSSW case, this configuration is unsustainable in the CDW case, where the ice shelf gets eroded and retreats to shallower, colder waters. We emphasize again that the presented results are steady state configurations and are not informative about possible transient responses.

[40] The results of experiment C are consistent with observations of thinning [*Shepherd et al.*, 2004] and increased melt rates [*Jacobs et al.*, 2011] of the PIG floating tongue. We thus speculate that changes of the PIG melt rates commonly attributed to changes in the shelf circulation [*Jacobs et al.*, 2011] may also be potentially triggered by changes in the PIG flow at the grounding line [*Joughin et al.*, 2003] or by changes in the thermocline [*Jacobs et al.*, 2011]. We point out, however, that since PIG and its floating tongue are not in steady state as considered here, its transient states triggered by the different mechanisms may have different configurations. It also remains to be seen whether the similarity of steady states caused by increased ice flux and shallowed thermocline depth holds in circumstances where the grounding line is dynamic.

5. Conclusions

[41] Using a coupled 1-D ice/ocean model and an analytic expression for ice shelf temperature, we have found that the oceanic environment in which ice shelves flow determines their states. Ice shelves flowing in cold, HSSW oceans differ from those in warm, CDW oceans in fundamental ways: their mass balance is controlled by different processes (ice advection and deformation in HSSW versus ice advection and melting in warm oceans), their thermal structure is different (warmer interior in cold oceans versus colder interior in the warm oceans), and they respond differently to different mechanisms that lead to the increase of the ocean heat content (higher sensitivity to warming of the cold bottom water versus higher sensitivity to shallowing the depth of the thermocline in the warm ocean). These findings suggest that ice shelves in different oceanic environments require treatments (e.g., modeling and observations) specific to each environment.

[42] In addition, we have established that the ice shelf/sub–ice shelf cavity systems are inherently coupled with strong feedbacks in geometry, melt rates, ice flow, and temperature. This fact has an important implication on the modeling treatments of these systems. Despite very large melt rates achieved near the grounding line in the warm, CDW ocean environment, simulations with the coupled model produce steady state configurations in which the effects of strong melting are compensated for by ice influx from the grounding line. However, such configurations cannot be simulated with uncoupled models where the ice shelf and cavity circulation components are treated separately. Assumptions of a static ice shelf in ocean-only simulations are justifiable only in circumstances where the ice shelf is close to steady state. A possible rule of thumb that determines whether an ice shelf/sub–ice shelf cavity system requires coupled treatment can be based on the leading order mass balance of an ice shelf: if it is between ice advection and deformation, then it is reasonable to apply ocean-only models; otherwise, a coupled ice/ocean model is required.

Appendix A: Analytic Treatment of Temperature in 2-D Ice Shelves

[43] In ice shelves with 2-D vertical cross section experiencing basal melting and zero net surface accumulation, the heat advection-diffusion equation written in terms of a stretched vertical coordinate $\zeta = \frac{z-b}{H}$ (i.e., equal to 0 at the ice shelf base and 1 at its surface) is as follows:

$$uT_x - \frac{T_\zeta}{H}(1-\zeta)\dot{b} = \frac{\kappa_i}{H^2}T_{\zeta\zeta} \tag{A1}$$

where x is the horizontal coordinate, $T(x,\zeta)$ is ice temperature, H is ice thickness, u is ice velocity, $\dot{b}$ is basal melt rate (positive for melting), and κ_i is the thermal diffusivity of ice [e.g., *MacAyeal and Thomas*, 1986; *MacAyeal*, 1997].

[44] Equation (A1) can be written in the following way:

$$qT_x + q_x(1-\zeta)T_\zeta = \frac{\kappa_i}{H}T_{\zeta\zeta} \tag{A2}$$

where q is ice shelf mass flux, $q = uH$. In steady state with zero net surface accumulation, the continuity equation simplifies to the following:

$$q_x = -\dot{b}. \tag{A3}$$

[45] Hence,

$$q(x) = q_g - \int_0^x dx'\dot{b}(x'), \tag{A4}$$

where q_g is ice flux at the grounding line.

[46] The nondimensional form of (32) is

$$\widetilde{q}\widetilde{T}_{\widetilde{x}} + \widetilde{T}_\zeta(1-\zeta)\widetilde{q}_{\widetilde{x}} = \frac{1}{\epsilon\widetilde{H}}\widetilde{T}_{\zeta\zeta} \tag{A5}$$

where $\widetilde{\ }$ denotes dimensionless variables that are chosen as follows: $\widetilde{T} = \frac{T}{[\Theta]}$, $\widetilde{x} = \frac{x}{[L]}$, $\widetilde{q} = \frac{q}{[Q]}$, $\widetilde{H} = \frac{H}{[H_0]}$ with scales $[\Theta] = T_g(1)$, $[Q] = q_g$, $H_0 = H_g$, $\epsilon = Pe$, and $Pe = \frac{H^2 u}{L\kappa_i}$ is the Peclet number. A solution of this equation can be written in a form

$$\widetilde{T}(\widetilde{x},\zeta) \approx \widetilde{T}^{[0]}(\widetilde{x},\zeta) + \theta(\widetilde{x},\eta) \tag{A6}$$

where $\widetilde{T}^{[0]}(\widetilde{x},\zeta)$ satisfies (A2) to the zeroth order in a small parameter ϵ^{-1} in the ice shelf interior ($\epsilon = Pe \gg 1$ in ice shelves), $\theta(x,\eta)$ is the temperature in a basal boundary layer, and η is the boundary layer coordinate $\eta = \epsilon^\alpha\zeta$. The equation for $\widetilde{T}^{[0]}$ is

$$\widetilde{q}\widetilde{T}^{[0]}_{\widetilde{x}} + \widetilde{T}^{[0]}_\zeta(1-\zeta)\widetilde{q}_{\widetilde{x}} \cong 0. \tag{A7}$$

[47] Its solution can be found by methods of characteristics:

$$\widetilde{T}^{[0]}(\widetilde{x},\zeta) = \widetilde{T}_g[\xi(\widetilde{x},\zeta)], \tag{A8}$$

where $\xi(\widetilde{x},\zeta) = 1 - \frac{1-\zeta}{\widetilde{q}_g}\widetilde{q}(\widetilde{x})$. Note that this solution satisfies the top surface boundary condition (under our assumptions, the top surface temperature is spatially uniform and is the same as at the grounding line); however, it does not satisfy the bottom surface boundary condition

$$\widetilde{T}|_{\zeta=0}(\widetilde{x}) = \widetilde{T}^*(\widetilde{x}) \tag{A9}$$

where T^* is the seawater freezing point, defined by equation (3). Ice temperature $\widetilde{T}$ is adjusted in the thermal boundary layer to satisfy this condition. Substitution of (A6) in (A5) yields the following equation for the boundary layer temperature $\theta(\widetilde{x},\eta)$:

$$\widetilde{q}\theta_{\widetilde{x}} + \theta_\eta\epsilon^\alpha(1-\epsilon^{-\alpha}\eta)\widetilde{q}_{\widetilde{x}} = \frac{\epsilon^{2\alpha-1}}{\widetilde{H}}\theta_{\eta\eta} + \frac{\epsilon^{-1}}{\widetilde{H}}\left(\frac{\widetilde{q}}{\widetilde{q}_g}\right)^2\widetilde{T}''_g(\xi) \tag{A10}$$

and boundary conditions

$$\theta(\widetilde{x},\eta) = \widetilde{T}^*(\widetilde{x}) - \widetilde{T}_g[\xi(\widetilde{x},0)] \tag{A11}$$

$$\theta(\widetilde{x},\eta\to\infty) = 0 \tag{A12}$$

[48] By choosing $\alpha = 1$ in (A10) and retaining only the highest-order terms, the above equation simplifies to

$$\theta_\eta \widetilde{q}_{\widetilde{x}} \widetilde{H} = \theta_{\eta\eta}. \tag{A13}$$

[49] A solution of (A13)–(A10) is

$$T_{bl}(x,\zeta) = \left\{T^*(x) - T_g[\xi(x,0)]\right\} e^{-\frac{\dot{b} H_\zeta}{\kappa_i}\zeta} \tag{A14}$$

where we took into account the ice shelf mass balance (A3) and returned to dimensional parameters. We point out that this solution is invalid for $\dot{b} \le 0$. Temperature in the ice shelf is

$$T(x,\zeta) = T_g[\xi(x,\zeta)] + T_{bl}(x,\zeta). \tag{A15}$$

Appendix B: Coupled Model Parameters

[50] We use the following parameters in the coupled model simulations. The temperature profile of ice flowing into the ice shelf (at the grounding line), $T_g(z)$, is the Robin solution [*Robin*, 1955] with 0.1 m year^{-1} surface accumulation and 48 W m^{-2} geothermal heat flux.

[51] We consider two oceanographic environments that have the same stratification

$$\Psi(z) = \begin{cases} \Psi_{sw} & z \ge -300 \text{ m} \\ \Psi_{bw} + \dfrac{\Psi_{sw} - \Psi_{bw}}{-300 - D_{tc}}(z + 300) & D_{tc} \le z < -300 \text{ m} \\ \Psi_{bw} & z < D_{tc} \end{cases} \tag{B1}$$

where Ψ stands for T or S, the subscript sw refers to the surface water properties, $T_{sw} = -1.9°\text{C}$, $S_{sw} = 33.5‰$, $D_{tc} = -800$ m is the thermocline depth, the subscript bw refers to the bottom water properties, where salinity $S_{sw} = 34.69‰$, temperature $T_{bw} = -1.8°\text{C}$ for the HSSW case and 1.2°C for the CDW case.

[52] For the plume model, the boundary conditions are such that the flux of the fresh water at the grounding line is 5×10^{-5} m^2 s^{-1}, the momentum flux is 5×10^{-7} m^3 s^{-2}, temperature is $-1.2°\text{C}$ (ice pressure melting point for thickness at the grounding line), and the salinity is 15‰. All other parameters of the plume model are the same as in *Jenkins* [1991].

[53] **Acknowledgments.** We thank Editor Bryn Hubbard, the Associate Editor Poul Christoffersen, and three anonymous referees for valuable comments and suggestions that improved clarity of the manuscript. We also thank Doug MacAyeal for useful discussions and help with this manuscript. O.V.S. is supported by NSF grants ANT-0838811, ARC-0934534. D.N.G. is supported by NSF grant ANT-1103375. C.M.L. is supported by the Princeton Carbon Mitigation Initiative.

References

Dupont, T. K., and R. B. Alley (2005), Assessment of the importance of ice-shelf buttressing to ice-sheet flow, *Geophys. Res. Lett.*, *32* 1–4, doi:10.1029/2004GL022024.

Engelhardt, H. (2004), Thermal regime and dynamics of the West Antarctic ice sheet, *Ann. Glaciol.*, *39*, doi:10.3189/172756404781814203.

Engelhardt, H., and J. Determann (1987), Borehole evidence for a thick layer of basal ice in the central Ross Ice Shelf, *Nature*, *327*, 318–319.

Gagliardini, O., G. Durand, T. Zwinger, R. C. A. Hindmarsh, and E. L. Meur (2010), Coupling of ice-shelf melting and buttressing is a key process in ice-sheets dynamics, *Geophys. Res. Lett.*, *37*, 1–5 doi:10.1029/2010GL043334.

Goldberg, D. N., C. M. Little, O. V. Sergienko, A. Gnanadesikan, R. Hallberg, and M. Oppenheimer (2012a), Investigation of land ice-ocean interaction with a fully coupled ice-ocean model, Part 1: Model description and behavior, *J. Geophys. Res.*, *117*, F02037, doi:10.1029/2011JF002246.

Goldberg, D. N., C. M. Little, O. V. Sergienko, A. Gnanadesikan, R. Hallberg, and M. Oppenheimer (2012b), Investigation of land ice-ocean interaction with a fully coupled ice-ocean model, Part 2: Sensitivity to external forcings, *J. Geophys. Res.*, *117*, F02038, doi:10.1029/2011JF002247.

Hindmarsh, R. C. A. (1999), On the numerical computation of temperature in an ice sheet, *J. Glaciol.*, *45*, 568–574.

Holland, D. M., and A. Jenkins (1999), Modeling thermodynamic ice-ocean interactions at the base of an ice shelf, *J. Phys. Oceanogr.*, *29*, 1787–1800.

Holland, P. R., A. Jenkins, and D. M. Holland (2008), The response of ice shelf basal melting to variations in ocean temperature, *J. Climate*, *21*, doi:10.1175/2007JCLI1909.1.

Hooke, R. L. (1981), Flow law for polycrystalline ice in glaciers: Comparison of theoretical predictions, laboratory data, and field measurements, *Ref. Geophys.*, *19*, 664–672.

Humbert, A., R. Greve, and K. Hutter (2005), Parameter sensitivity studies for the ice flow of the Ross Ice Shelf, Antarctica, *J. Geophys. Res.*, *110*, F04022, doi:10.1029/2004JF000170.

Jacobs, S. S., A. L. Gordon, and J. R. Ardai, Jr. (1979), Circulation and melting beneath the Ross Ice Shelf, *Science*, *203*, 439–443, doi:10.1126/science.203.4379.439.

Jacobs, S. S., A. Jenkins, C. F. Giulivi, and P. Dutrieux (2011), Stronger ocean circulation and increased melting under Pine Island Glacier ice shelf, *Nat. Geosci.*, *4*, 519–523, doi:10.1038/ngeo1188.

Jenkins, A. (1991), A one-dimensional model of ice shelf-ocean interaction, *J. Geophys. Res.*, *96*, 20,671–20,677.

Jenkins, A., and C. S. M. Doake (1991), Ice-ocean interaction on Ronne Ice Shelf, Antarctica, *J. Geophys. Res.*, *96*, 791–813.

Jenkins, A., and S. Jacobs (2008), Circulation and melting beneath George VI Ice Shelf, Antarctica, *J. Geophys. Res.*, *113*, C04013, doi:10.1029/2007JC004449.

Jenkins, A., H. F. J. Corr, K. W. Nicholls, C. L. Stewart, and C. S. M. Doake (2006), Interactions between ice and ocean observed with phase-sensitive radar near an Antarctic ice-shelf grounding line, *J. Glaciol.*, *52*, 325–346, doi:10.3189/172756506781828502.

Joughin, I., and L. Padman (2003), Melting and freezing beneath Filchner-Ronne Ice Shelf, Antarctica, *Geophys. Res. Lett.*, *30*(9), 1–19, doi:10.1029/2003GL016941.

Joughin, I., E. Rignot, C. E. Rosanova, B. K. Lucchitta, and J. Bohlander (2003), Timing of recent accelerations of Pine Island Glacier, Antarctica, *Geophys. Res. Lett.*, *30*(13), 1–13, doi:10.1029/2003GL017609.

Liu, H. W., and K. J. Miller (1979), Fracture toughness of fresh water ice, *J. Glaciol.*, *22*, 135–143.

MacAyeal, D. (1984), Thermohaline circulation below the Ross Ice Shelf: A consequence of tidally induced vertical mixing and basal melting, *J. Geophys. Res.*, *89*, 597–606.

MacAyeal, D. (1997), EISMINT: Lessons in ice-sheet modeling, unpublished lecture notes, http://geosci.uchicago.edu/pdfs/macayeal/lessons.pdf.

MacAyeal, D. R. (1989), Large-scale ice flow over a viscous basal sediment—Theory and application to Ice Stream-B, Antarctica, *J. Geophys. Res.*, *94*, 4071–4087.

MacAyeal, D. R., and V. Barcilon (1988), Ice-shelf response to ice-stream discharge fluctuations: I. Unconfined ice tongues, *J. Glaciol.*, *34*, 121–127.

MacAyeal, D. R., and R. H. Thomas (1986), The effects of basal melting on the present flow of the Ross Ice Shelf, Antarctica, *J. Glaciol.*, *32*, 72–86.

Nicholls, K. W., S. Osterhus, K. Makinson, and M. R. Johnson (2001), Oceanographic conditions south of Berkner Island, beneath Filchner-Ronne Ice Shelf, Antarctica, *J. Geophys. Res.*, *106*, 11,481–11,49.

Orheim, O., J. O. Hagen, and A. C. Sætrang (1990), Glaciologic and oceanographic studies on Fimbulisen during NARE, *Tech. Rep. 4*, FRISP.

Robin, G. d. Q. (1955), Ice movement and temperature distribution in glaciers and ice sheets, *J. Glaciol.*, *2*, 523–532.

Schoof, C. (2007), Ice sheet grounding line dynamics: Steady states, stability, and hysteresis, *J. Geophys. Res.*, *112*, F03S28, doi:10.1029/2006JF000664.

Shepherd, A., D. Wingham, T. Payne, and P. Skvarca (2003), Larsen Ice Shelf has progressively thinned, *Science*, *302*(5646), 856–859.

Shepherd, A., D. Wingham, and E. Rignot (2004), Warm ocean is eroding West Antarctic Ice Sheet, *Geophys. Res. Lett.*, *31*, L23402, doi:10.1029/2004GL021106.

Zotikov, I. A., V. S. Zagorodnov, and J. V. Raikovsky (1980), Core drilling through the Ross Ice Shelf (Antarctica) confirmed basal freezing, *Science*, *207*, 1463–1465.